PERFORMANCE ANALYSIS OF SPACEBORNE SAR VEHICLE DETECTION AND VELOCITY ESTIMATION

Franz Meyer[‡], Stefan Hinz[†], Andreas Laika[†], Steffen Suchandt[‡], Richard Bamler[†,‡]

[†]Remote Sensing Technology, Technische Universitaet Muenchen, Arcisstr. 21, D - 80333 Muenchen, Germany
[‡]Remote Sensing Technology Institute, German Aerospace Center (DLR), Oberpfaffenhofen, D - 82234 Wessling, Germany

Commission III/5

ABSTRACT:

With TerraSAR-X and RADARSAT-2, two dual-channel SAR satellites will be launched in the next months. Both sensors allow for detecting moving objects, and, by this, enable traffic monitoring from space. This paper revises the theoretical background of traffic monitoring with space-based SARs and presents concepts for the TerraSAR-X traffic monitoring system. Compared to previous work an extensive analytical and empirical accuracy analysis is included for both vehicle detection and velocity estimation. The accuracy analysis includes a theoretical accuracy evaluation and a validation with real data.

1 INTRODUCTION

Since the launch of new optical satellite systems, e.g. Ikonos and QuickBird, satellite imagery with 1-meter resolution or higher is commercially available and a number of approaches have been developed to detect or track vehicles in this imagery (see e.g. references in (Leitloff et al., 2005)). Traffic monitoring based on optical satellite systems, however, is only possible at daytime and cloud-free conditions. Two high-resolution Spaceborne RADAR systems, TerraSAR-X (Germany) and RADARSAT-2 (Canada), which will be launched this year will overcome this limitations. Yet there are other difficulties inherent in the SAR imaging process that must be solved to design a reasonably good approach for traffic monitoring using spaceborne Radar.

The task of detecting moving vehicles with SAR sensors (ground moving target indication (GMTI)) has been addressed in several scientific publications. The method of choice in GMTI is to use a Radar or SAR sensor with at least 3 channels and use space-time adaptive processing (STAP) for target detection. Further reference to that topic can be found e.g. in (Klemm, 1998, Livingstone et al., 2002, Gierull, 2004). Unfortunately, civilian space borne SAR systems with 3 or more channels are currently not available. The upcoming TerraSAR-X mission as well as the Canadian RADARSAT-2 mission will be equipped with a single channel SAR that can be switched to an experimental mode with two channels to enable along-track interferometric applications like traffic monitoring. Although the use of a 2-channel system is not optimal for detecting vehicles, some methods exist that allow detection under certain conditions. The classical approach to do so is to use the displaced phase center array (DPCA) method. Along-track interferometry (ATI) is another method that can be used. The issue of detecting moving targets using ATI is for instance discussed in (Gierull, 2001, Sikaneta and Gierull, 2005). In (Gierull, 2002) special emphasis is put on the probability density functions associated with this detection. The influence of vehicle acceleration is discussed in (Sharma et al., 2006). Traffic monitoring from space is quite rare so far. But as shown in (Breit et al., 2003, Meyer and Hinz, 2004, Meyer et al., 2005) first endeavors have already been carried out.

Based on a revision of the effects of moving objects in SAR Data we present a concept of detection and velocity estimation of vehicles, thereby considering the restrictions of *civilian* SAR satellite systems. The main focus of this paper, finally, lies on the performance characterization of the main components of this concept, in order to predict and validate the expected results of the system for TerraSAR-X. The performance analysis includes both a theoretical accuracy evaluation and a validation with real airborne SAR data.

2 MOVING OBJECTS IN SPACEBORNE SAR IMAGES

Before outlining the concepts for vehicle detection and velocity estimation we briefly summarize the effects of moving objects in spaceborne SAR images. Here, only the resulting formulae are included; a derivation of the formulae can be found, e.g. in (Meyer et al., 2005), while a comprehensive overview on SAR image processing is given in (Cumming and Wong, 2005).

2.1 Object Motion Effects in SAR — A Summary

The position of a Radar transmitter on board a satellite is given by $P_{sat}(t) = [x_{sat}(t), y_{sat}(t), z_{sat}(t)]$ with x being the along-track direction, y the across-track ground range direction and z being the vertical. A point scatterer is assumed to be at position $P_{mover} = [x_{mover}(t), y_{mover}(t), z_{mover}(t)]$, and the range to this arbitrarily moving and accelerating point target from the radar platform is defined by $R(t) = P_{sat}(t) - P_{mover}(t)$.

Omitting pulse envelope, amplitude, and antenna pattern for simplicity reasons, and approximating the range history $R(t)$ by a parabola, the measured echo signal $u(t)$ of a static point scatterer can be written as

$$u_{stat}(t) = \exp\{j\pi FM t^2\} \tag{1}$$

with

$$FM = -\frac{2}{\lambda}\frac{d^2}{dt^2}R(t) = -\frac{2}{\lambda R}v_{sat}v_B \tag{2}$$

being the frequency modulation (FM) rate of the azimuth chirp. Azimuth focussing of the SAR image is performed using the matched filter concept(Bamler and Schättler, 1993, Cumming and

Wong, 2005). According to this concept, an optimally focused image is obtained by complex-valued correlation of $u_{stat}(t)$ with the filter $s(t) = \exp\{-j\pi FM t^2\}$. To construct $s(t)$ correctly, the actual range history of each target in the image, and thus, the position and motion of sensor and scatterer, must be known. Usually, the time dependence of the scatterer position is ignored yielding $P_{mover}(t) = P_{mover}$. This concept is commonly referred to as *stationary-world matched filter* (SWMF). Because of this definition, a SWMF does not correctly represent the phase history of a significantly moving object, which eventually results in image deteriorations.

We first evaluate targets moving with velocity v_{y0} in *across-track* direction. This movement causes a change of range history proportional to the projection of the motion vector into the line-of-sight direction of the sensor $v_{los} = v_{y0} \cdot sin(\theta)$, with θ being the local incidence angle. In case of constant motion during illumination the change of range history is linear and causes an additional linear phase trend in the echo signal. The resulting signal of an object moving in line-of-sight direction with velocity v_{los} is consequently:

$$u(t) = \exp\{j\pi FM t^2\} \cdot \exp\left\{-j\frac{4\pi}{\lambda}v_{los}t\right\} \qquad (3)$$

If $u(t)$ is focused with the SWMF $s(t)$ defined above, the linear phase term in Equ. (3) is not compensated for, and remains in the phase of the focused signal. This linear phase term corresponds to a shift of the signal in space domain, which is given by

$$\Delta az = -R\frac{v_{los}}{v_{sat}} \quad [m] \qquad (4)$$

According to Equ. (4), across-track motion results in an along-track displacement of the moving object. It is displaced in flying direction if the object moves towards the sensor and reverse to flying direction if the movement is directed away from the sensor. When inserting the TerraSAR-X parameters into the above formulae, one can see, that moving vehicles are displaced significantly from their real position even for small across-track velocities (about $1\,km$ for $50\,km/h$ at $45°$ inc. angle). This effect strongly hampers the recognition of cars in TerraSAR-X images as their position is not anymore related to semantic information, e.g. streets. A detailed analysis and illustration of these effects is given in (Meyer et al., 2005).

The target is now assumed to move with velocity v_{x0} in *along-track*. In this case the relative velocity of sensor and scatterer is different for moving objects and surrounding terrain. Thus, along-track motion changes the frequency modulation (FM) rate of the received scatterer response. The FM rate FM_{mt} of a target moving in along-track with velocity v_{x0} is defined by $FM_{mt} = FM\left(1 - \frac{v_{x0}}{v_B}\right)$. If the echo signal of this object is focused with a SWMF $s(t)$, a quadratic phase component remains in the focused signal leading to a spread of the signal energy in time or space domain. The width of the focused peak as a function of the object's along-track velocity v_{x0} can be approximated by

$$\Delta t \approx 2T_A\sqrt{\frac{v_{sat}}{v_B}}\frac{v_{x0}}{\sqrt{v_{sat}v_B}} \quad [s] \qquad (5)$$

with T_A being the aperture time. Interpretation of Equation (5) shows that a moving vehicle is smeared by twice the distance it moved along track during the illumination time T_A. Note that the approximation in Equation (5) only holds for $v_{x0} \gg 0$. As the backscattered energy of the moving object is now spread over a larger area the peak value of the signal drops down. Using the

parameter set of TerraSAR-X, it is obvious that blurring and peak power decrease are quite drastic. The strong blurring distributes the backscattered energy and results in a drop of $50\,\%$ peak power or more if $v_{x0} \geq 15\,km/h$ (Meyer et al., 2005). Thus, nearly all ground moving targets suffer from energy dispersion, which decreases the signal-to-clutter ratio and renders target detection more difficult.

Similar analyses are conducted for first order accelerations. Such effects not only appear if drivers physically accelerate or brake but also along curved roads, as the object's along-track and across-track velocity components vary during illumination time. The analysis is based on a third order Taylor series expansion of the range $R(t)$ to an accelerating and isotropic point scatterer. The scatterer is assumed to be at position $(0, y_0, 0)$ at azimuth time $t = 0$ and to move with velocity $(v_{x0}, v_{y0}, 0)$ and acceleration $(a_x, a_y, 0)$. With R_0 being the range at azimuth time $t = 0$ the third order Taylor series expansion of $R(t)$ calculates to:

$$R(t) \approx R_0 + \frac{y_0 v_{y0}}{R_0}t - \frac{1}{2R_0}\left[\frac{y_0 v_{y0}(v_{x0}-v_{sat})^2 + y_0 v_{y0}^3}{R_0^2}\right]t^3 +$$

$$\frac{1}{2R_0}\left[y_0 a_{y0}\left(1 - \frac{y_0^2}{R_0^2}\right) + (v_{x0} - v_{sat})a_{x0}\right]t^3 +$$

$$\frac{1}{2R_0}\left[(v_{x0} - v_{sat})^2 + v_{y0}^2\left(1 - \frac{y_0^2}{R_0^2}\right) + y_0 a_{y0}\right]t^2 \qquad (6)$$

It can be seen in Equation (6) that acceleration components appear in the quadratic and the cubic term of the Taylor series expansion. The acceleration in across-track direction (a_y) causes a quadratic phase component, which results in a spread of the signal energy in time or space domain. Considering the TerraSAR-X system parameters it comes clear that image degradation due to across-track accelerations is significant for $a_y > 1\,\frac{m}{s^2}$, which is commonplace for traffic on roads or highways (Meyer et al., 2005). On the other side, along-track acceleration a_x appears only in the cubic term of Equation (6) and results in an asymmetry of the focused point spread function. For TerraSAR-X, this effect is very small even for unrealistic accelerations, and can be neglected.

2.2 Detection Approaches

On one hand, all the above described effects of moving objects hinder the detection of cars in conventionally processed SAR images. On the other hand, these effects are mainly deterministic and can be exploited to not only detect vehicles but also measure their velocity. Our system for moving object detection consists of two major components: a detection and a velocity estimation component. Both components make use of a-priori knowledge in form of a road database and expectation values for the aspect-angle dependent Radar cross-section of vehicles. In the following sections we discuss the approaches employed in the system in more detail.

In order to detect moving objects in SAR data one has to predict their appearance in the image. Thus, the main tasks to solve are the *estimation* of the blurring, the displacement, and the interferometric phase values associated with the particular moving object. The solution to this typical inverse problem can be facilitated when incorporating a priori knowledge about the appearance, location, and velocity of vehicles. Hence, we will first turn to the integration of a priori knowledge (Sect. 2.2.1) before describing different detection approaches in Sects. 2.2.2, 2.2.3 and 2.2.4.

2.2.1 Integration of A-priori Information

Assuming objects being point scatterers and given the SAR- and platform parameters, the displacement effect in the along-track direction can be predicted when real position, velocity, and motion direction of the vehicle are known. Because of the functional relation of interferometric phase and object velocity in across-track direction, also the interferometric phase of a displaced moving object can be derived (see below).

In our case, road network databases serve as basic source for acquiring a priori knowledge. Typically, these databases contain road axes in form of polygons and attributes like road class, road width, maximum velocity, etc. attached to each polygon. Using this information a number of "maps" representing the a priori information can be derived (i.e. displacement map, velocity map, and interferometric phase map). Figure 1 shows an example for the different maps derived for a single road segment.
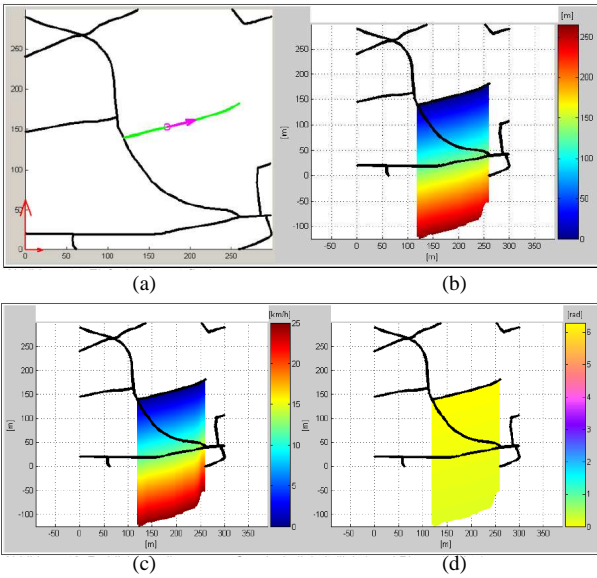
Figure 1: Example for maps derived from a single road segment associated with travelling direction (see (a)): (b) Displacement map, (c) velocity map, (d) phase map.

Besides the information about the phase, also a priori information about the vehicle's radar cross section strongly supports detection. As it is well known, significant variations of radar cross section exist over different aspect angles of cars. An example of radar cross section variations as a function of aspect angle α for a Volkswagen Golf car derived from experimental measurements of DLRs airborne SAR system E-SAR is shown in Fig. 2. The analysis of the RCS curve shows that cars have quite high RCS values if their front, rear or side faces the sensor. RCS values for the angles around $45°$ and $135°$ are significantly lower. It also can be seen that the RCS is subject to high variation even for small changes of aspect angle. Such information is incorporated into the detection scheme with the help of a road database, since—given the sensor and platform parameters—the aspect angle under which a car must have been illuminated by the sensor can be calculated for each road segment.

2.2.2 Along-Track Interferometry

In along-track interferometry (ATI) an interferogram I is formed from two original SAR images acquired with a short time lag in along-track direction. The interferogram phase can be related to object motion by:

$$\psi = \frac{4\pi}{\lambda}\Delta R = \frac{4\pi}{\lambda}v_{los}t = \frac{4\pi}{\lambda}v_{los}\frac{\Delta l}{v_{sat}} \qquad (7)$$
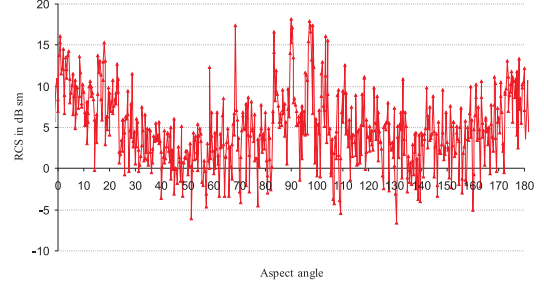
Figure 2: Radar cross section depending on aspect angle. Experimental data of a VW Golf car in X-band.

where t is the temporal separation of the aquisitions defined by the satellite motion and the effective distance Δl between the phase centers of the two antennas. Since both interferometric phase ψ and azimuth displacement Δaz are caused by across-track motion, an analytic relation between both measurements can be established:

$$\Delta az = -R\frac{v_{los}}{v_{sat}} = -R\psi\frac{\lambda}{4\pi\Delta l} \qquad (8)$$

To design a constant false alarm rate (CFAR) detection scheme, the probability density distributions of vehicles and background in interferometric data need to be known. Here, we follow the derivation presented in (Lee et al., 1994) and (Joughin et al., 1994). For all stationary targets the interferometric phase values are assumed to be statistically distributed around the expectation value $E[\psi] = 0$. Using the underlying assumption of jointly Gaussian-distributed data in the two images, the joint probability density function (pdf) $f_c(\eta, \psi)$ of amplitude and phase of an interferogram is given by:

$$f_c(\eta,\psi) = \frac{2n^{n+1}\eta^n}{\pi\Gamma(n)\left(1-|\rho|^2\right)}\exp\left(\frac{2n\eta|\rho|\cos(\psi)}{1-|\rho|^2}\right)K_{n-1}\left(\frac{2n\eta}{1-|\rho|^2}\right) \quad (9)$$

where n is the number of looks (effectively the amount of averaging), $\Gamma(\cdot)$ is the gamma function and $K_n(\cdot)$ is the modified Bessel function of the nth kind. For medium resolution SAR the jointly Gaussian assumption has been validated for most agricultural and vegetated areas (Ulaby and Dobson, 1989). As outlined in Sect. 2.2.1 it is possible to derive expectation values for position, interferometric phase, and aspect-dependent radar cross section of vehicles using ancillary data. Hence, from these data also a pdf for "clutter+mover" $f_{c+m}(\eta, \psi)$ should be established. An approximation valid for $n \gg 1$ has been derived in (Gierull, 2002) and is given by:

$$f_{c+m}(\eta,\psi) = \frac{2n^{n+1}\eta\left((\eta-\delta\cos(\zeta))^2+\delta^2\sin(\zeta)^2\right)^{\frac{n-1}{2}}}{\pi\Gamma(n)\left(1-|\rho|^2\right)} \cdot$$
$$\exp\left(\frac{2n\rho(\eta\cos(\psi)-\delta\cos(\vartheta))}{1-\rho^2}\right)K_{n-1}\left(\frac{2n\sqrt{(\eta-\delta\cos(\zeta))^2+\delta^2\sin(\zeta)^2}}{1-\rho^2}\right) \quad (10)$$

while the moving target's signal is assumed to have a peak amplitude β, and with $\delta = \frac{\beta}{\eta}$ and $\zeta = \psi - \vartheta$. Using this approximation as an alternative hypothesis, $f_{c+m}(\eta, \psi)$ allows to define a likelihood ratio to which a threshold can be applied.

Figure 3a) shows a typical example of $f_c(\eta, \psi)$ assuming a coherency of $|\rho| = 0.95$, $n = 1$ and a expected signal amplitude of $E[\eta] = 1$, while Fig. 3b) shows an example of $f_{c+m}(\eta, \psi)$ and a corresponding curve of separation.

2.2.3 Displaced Phase Center Array Method

In a similar way one may derive a CFAR detector based on the displaced
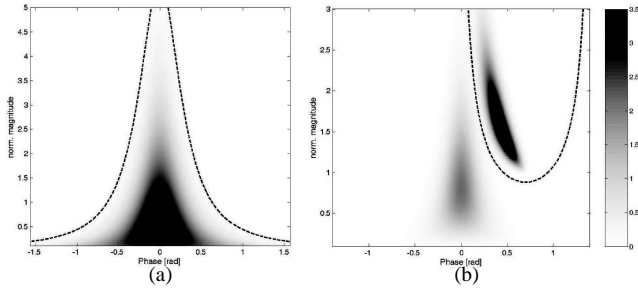
Figure 3: PDFs for background only (a) and background as well as moving objects (b). The dashed line is an example for curve of separation.

phase center array (DPCA) technique, where the two coregistered images are simply substracted, yielding

$$
\begin{aligned}
I_{DPCA} &= I_1 - I_2 = |I_{DPCA}| \cdot (e^{j\phi_1} - e^{j\phi_2}) \\
&= 2|I_{DPCA}|sin(\frac{\phi_1 - \phi_2}{2})e^{j\left(\frac{\phi_1-\phi_2}{2}+\frac{\pi}{2}\right)} \quad (11)
\end{aligned}
$$

Here, only the magnitude $2|I_{DPCA}|sin(\frac{\phi_1-\phi_2}{2})$ of the signal is evaluated for classification. Hence, the above pdf's simplify to a one-dimensional case. The magnitude of I_{DPCA} is high whenever moving objects cause a phase shift between the two images and low if the observed surface elements are stable.

2.2.4 Frequency Modulation Method The approaches outlined so far can only be applied if displacement or interferometric phase occurs at all. This does not happen for objects moving purely in azimuth (along-track) direction. As explained in Sect. 2.1 such vehicles appear defocussed in the image. Focusing these objects is however possible when choosing a FM rate that corresponds to the relative velocity of platform and object. Our strategy for finding the correct FM rate relies on hypothesizing a series of FM rates and analyzing a pixel's "sharpness function" over these FM rates (see (Weihing et al., 2006) for details). Since blurring occurs only in azimuth direction, searching the correct FM rate for a given pixel reduces to a 2D-problem. Moreover, the known location of roads as well as the expected range of vehicle velocities allow to further restrict the search space to a limited number of FM rates. For extracting the energy peak, we implemented a simple but effective blob detection scheme that analyzes the local curvatures in azimuth- and FM-direction, thereby incorporating a certain amount of smoothing depending on the expected noise level of the images. Combining local curvature maxima and peak amplitude by the geometric mean yields the final decision function, from which the maximum is selected (see (Hinz, 2005) for details). The FM-rate at the extracted peak corresponds to the correct along-track velocity – assuming that target acceleration can be neglected for a first guess.

2.3 Velocity Estimation

The estimation of the velocity of detected vehicles can be done based on all effects moving objects cause in SAR images and SAR interferograms. Thus, approaches may use *i)* the interferometric phase values, *ii)* the displacement of detected vehicles from their corresponding roads, and *iii)* the along-track defocus caused by along-track motion and/or across-track acceleration. All possible approaches have their advantages and disadvantages and differ in the accuracy of their results (see Sect. 4). The presence of several methods for estimating velocities leads to an over-determination of the estimation problem. This redundancy might

be used to estimate across-track acceleration in addition to the vehicle's velocity. However, this has not yet been realized in the current implementation of the system.

3 PERFORMANCE ANALYSIS OF DETECTION

In order to assess the detection performance for varying scenarios, three different approaches have been used: *i)* an analytical performance analysis based on analytical pdf's and Receiver Operator Characteristic (ROC) curves obtained therefrom (Sect. 3.1); *ii)* a numerical performance analysis derived from simulations (Sect. 3.2); and *iii)* a performance analysis based on data from airborne SAR experiments. The system parameters are tuned to produce images that correspond to the expected space-borne data. In the following, we concentrate mainly on the detection based on the across-track components of vehicle motion. Analyses of the FM-Rate method described in Sect. 2.2.4 are given in (Weihing et al., 2006).

3.1 Analytical Performance Analysis of Detection

The analytical performance analysis is based on the pdf's given in Equs. 9 and 10 and shown in Fig. 3b). These pdf's allow for the calculation of detection and false-alarm probabilities for a given line of separation, i.e. a predefined likelihood ratio, see Fig. 4a). Thereby each parameterization of the pdf's corresponds to different characteristics of background and vehicle appearance. Finally, ROC-curves are obtained when varying the likelihood ratio. Figure 4a) depicts an example for a typical parameterization of the pdf's and Fig. 4b) shows the corresponding ROC curve. However, one has to keep in mind that a number of simplifications have been necessary to obtain the analytical pdf's, most notably the restriction to more than 3 looks and the precondition of Gaussian distributed clutter. Hence, although this approach allows for maximum flexibility, a ROC curve derived this way is only valid for open and rural areas.
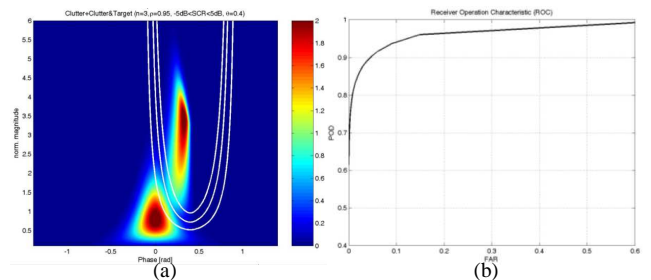
Figure 4: Analytical Detection Characterization: (a) Analytic PDFs $f_c(\eta,\psi)$, $f_{c+m}(\eta,\psi)$ and varying curves of separation. (b) Corresponding ROC curve.

3.2 Numerical Performance Analysis of Detection

To extent the analysis and to overcome some of the above limitations, a simulator for ATI and DPCA has been developed, which can be parameterized in such a way that a priori information about the interferometric phase and amplitude can be integrated. To generate a random sample, the whole process of data acquisition is simulated for both vehicles and clutter, i.e., the SAR-Data-Acquisition process, multilooking if required, and the generation of interferograms. Then, for each set of random samples a histogram is computed substituting the probability density functions. As above, to evaluate the performance of the detectors, a threshold is varied and the probability of detection and probability of

false alarm are determined for each step of this variation. Figure 5 illustrates the detection probability using ATI (a) and DPCA (b) over different vehicle velocities (i.e. phases) for certain vehicle brightnesses as well as fixed background and false alarm rate. As can be seen, for low velocities and bright vehicles ATI delivers generally better results while for faster vehicles it is outperformed by DPCA. The reason for this behavior is that DPCA purely relies on the interferometric phase, i.e., for low phase values the detection is strongly influenced by noise, which leads to the significant decrease of performance. In contrast, ATI makes also use of the amplitude so that, for low velocities, one additional feature is still left to detect a vehicle.
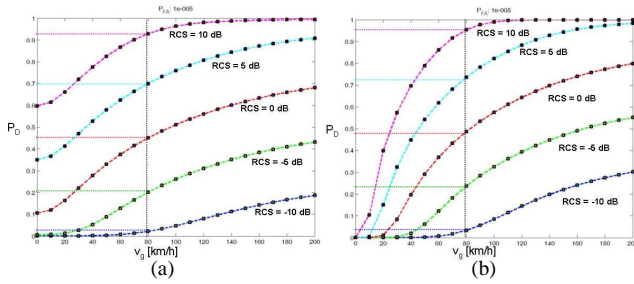
Figure 5: Numerical Detection Characterization: Detection Probabilities for given Background Clutter (bushes) and fixed False Alarm Rate (10e-5) calculated for varying vehicle brightnesses (RCS). (a) Results for ATI. (b) Results for DPCA.

3.3 Performance Analysis Based on Airborne Data

The validity of the simulation results has been assessed using real data of flight campaigns. Besides of this, tests on real data sets also allow to discover bottlenecks of the techniques employed and to reveal unforeseen problems. An additional goal is to simulate TerraSAR-X data for predicting the performance of the extraction procedures. To this end, an airborne Radar system has been used that has been modified so that the resulting raw data is comparable with future satellite data of TerraSAR-X. We followed two different ways of assessment: *i)* using real background data and, to have a "ground-truth", vehicles that have been artificially impainted into the background (Sect. 3.3.1) , and *ii)* detection of real vehicles in scenes for which optical data has been simultaneously acquired.

3.3.1 Background Data and Impainted Vehicles Figure 6a) shows a larger SAR scene composed of different types of background. In two test areas, vehicles in form of point targets have been impainted. The appearance of a vehicle (amplitude and phase) has been randomized using a random generator. Since in this case ground-truth is available one is able to obtain completeness and correctness curves when varying the detection threshold, which replace the detection and false alarm rates before. Figure 6b) shows these curves for a typical image background using a fixed vehicle velocity, statistically distributed vehicle brightness and DPCA as detection method. Although not being directly comparable with Fig. 5b), the typical behavior of DPCA is confirmed also by this evaluation, i.e., there is a striking lock-in of the quality of the results depending on the detection threshold.

3.3.2 Vehicle Detection in Airborne Data In the following, results of a flight campaign are shown during which images over real-life traffic scenarios on highways were acquired. To evaluate the results of SAR-based vehicle detection, time series of aerial photographs have been taken – almost synchronized with the SAR acquisition.
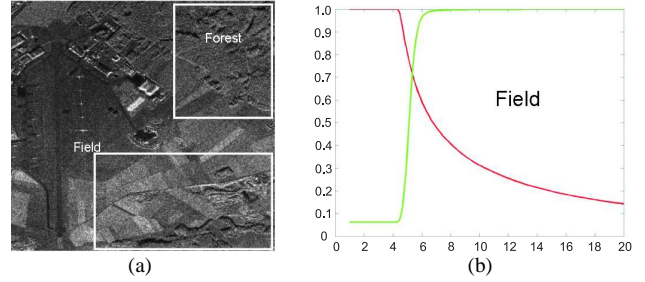
Figure 6: Detection Characterization based on airborne background image (a) and impainted vehicles with $RCS = 3dB \pm 8dB$ and phase according to 65km/h: Curves for completeness (red) and correctness (green) for agricultural area obtained by DPCA with varying thresholds.
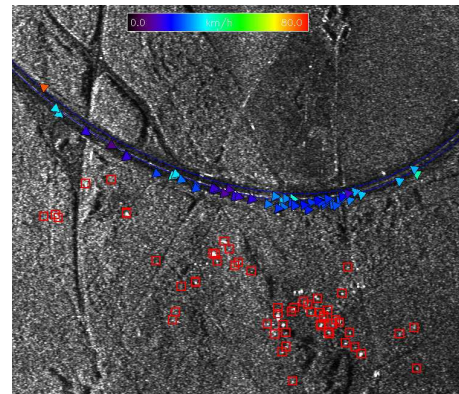
Figure 7: Experiments with airborne SAR: Detection results and velocity estimation for a dense traffic scenario

First encouraging results have been achieved with the system described above, although we have to admit that too few scenes have been processed up to now to give reliable and statistically confirmed statements about the system's performance. The used experimental proccesing system includes a combination of an ATI and a DPCA detector, and allows for an automatic integration of a-priori knowledge (NavTeq road data). It performs velocity estimation based on ATI phase and on along-track displacement. The incorporated road data not only enables displacement measurements but also the prediction of displacement intervals and thus a limitation of the search space. Typical results are depicted in Figure 7. It shows the detector performance for rather dense traffic. Although simultaneously acquired optical images are available for this scene, it was–due to unknow time delays–unfortunately not possible to match the car reference data form optical images uniquely to the detection results. Yet the evaluation of these results based on traffic flow parameters has shown that flow parameters can be derived precisely, although the completeness of detected cars is only moderate ((Suchandt et al., 2006)).

Figure 8 illustrates the detection of vehicle by FM-rate variation. The azimuth direction points from bottom to top, thus, along-track velocity components of vehicles travelling along the main road in the center of the image are quite small and moving vehicles are both blurred and displaced. At the bottom of Figure 8 a) the marked image patch is focused with FM rates corresponding to $0km/h$ and $15km/h$ (assuming absence of acceleration). As can be seen, the background of the image blurs for the second case, while one bright point gets sharp (marked by red arrows). Figure 8 b) shows the corresponding FM-slice, the detected peak, and an estimated along-track velocity of approx. $10km/h$ as-

suming zero acceleration. Considering a road orientation of 15 degree the vehicle velocity computes to approximately $40km/h$, which fits reasonably well to the velocity computed from the displacement ($37km/h$).

Scene (0 km/h)   Scene (-15 km/h)

(a)

$v_{x0} = -10.5$ km/h

(b)
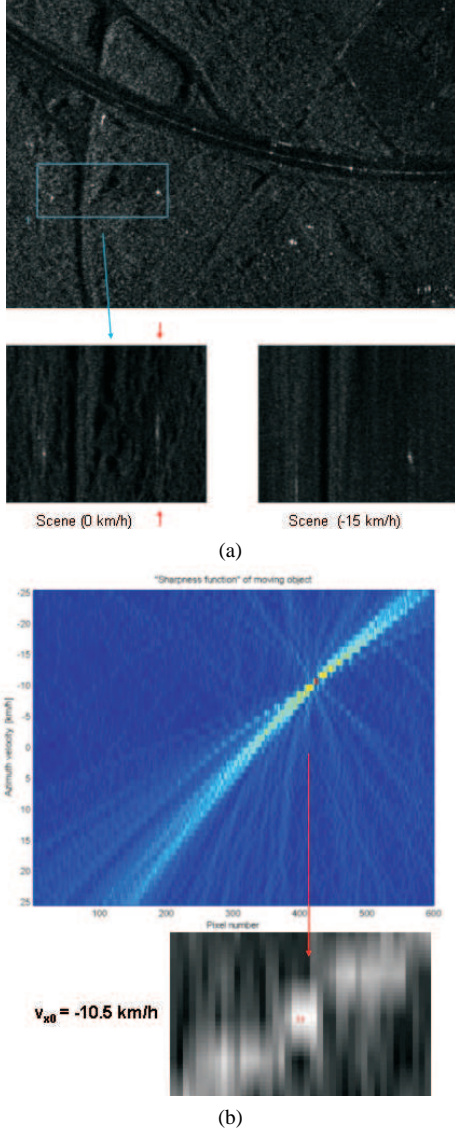
Figure 8: (a) Image patch (blue rectangle) focused with two different FM-rates (bottom). Red arrows mark azimuth line in which the sharpened point lies. (b) FM slice computed for this azimuth line (top) and detected peak (bottom).

4 PERFORMANCE ANALYSIS OF VELOCITY ESTIMATION

For each of the three approaches for velocity estimation, i.e. *i)* via interferometric phase, *ii)* via displacement, and *iii)* via along-track blurring, the corresponding accuracy values are derived, and at the end of this section, an example for accuracy when combining approaches is given.

4.1 Velocity Estimation based on the Interferometric Phase

The interferometric phase allows for a direct access to the objects line-of-sight velocity component without the need of auxiliary information. Still, information about the relative orientation of the road axis corresponding to the particular vehicle is needed in

order to derive the real heading velocity of vehicles from their line-of-sight motion. If we assume that a detected vehicle acts as point scatterer, the standard deviation σ_ψ of its interferometric phase is defined by

$$\sigma_\psi - \psi \approx \frac{1}{\sqrt{2 \cdot SCR}} \quad (12)$$

with *SCR* being the signal-to-clutter ratio of a point like target. SCR values can be determined based on RCS measurements of vehicles, which are shown in Sect. 2.2.1. Given Equation (12), the standard deviation of the derived across-track velocity estimate $\hat{v}_y^\psi$ results in

$$\sigma_{\hat{v}_y^\psi} = \frac{sin(\theta_{inc}) \cdot \lambda \cdot v_{sat}}{\sqrt{2 \cdot SCR} \cdot 4\pi \cdot \Delta l} \quad (13)$$

Given the system parameters of TerraSAR-X and assuming a SCR of 5 dB we get a standard deviation $\sigma_{\hat{v}_y^\psi}$ of approximately 30 km/h for the center of the TerraSAR-X swath. Clearly, for an analysis of traffic behavior and traffic dynamics, this accuracy level is only marginally sufficient.

4.2 Velocity Estimation from Along-track Displacement

Besides of the above mentioned approach, the heading velocity of a moving vehicle $\hat{v}_{mt}$ can be derived by measuring its along-track displacement from its corresponding road segment. The functional relation is given by

$$\hat{v}_{mt}^{\Delta az} = \frac{\hat{\Delta}az \cdot v_{mt}}{R \cdot sin(\hat{\alpha}_{road}) \cdot sin(\theta_{inc})} \quad (14)$$

where $\hat{\Delta}az = |\hat{x}_{road} - \hat{x}_{mt}|$ is the along-track displacement. The accuracy $\sigma_{\hat{v}_{mt}^{\Delta az}}$ of the velocity estimate is a function of the quality of the displacement measurement $|\hat{x}_{road} - \hat{x}_{mt}|$, and the accuracy of the road's heading angle $\hat{\alpha}_{road}$ relative to the satellite track. $\sigma_{\hat{v}_{mt}^{\Delta az}}$ is calculated by error propagation.

$$\sigma_{\hat{v}_{mt}^{\Delta az}} = \sqrt{\left(\frac{\partial \hat{v}_{mt}^{\Delta az}}{\partial x_{obj}}\right)^2 \sigma_{x_{obj}}^2 + \left(\frac{\partial \hat{v}_{mt}^{\Delta az}}{\partial x_{road}}\right)^2 \sigma_{x_{road}}^2 + \left(\frac{\partial \hat{v}_{mt}^{\Delta az}}{\partial \alpha_{road}}\right)^2 \sigma_{\alpha_{road}}^2} \quad (15)$$

From empirical evaluations of the peak detection approach we assessed the accuracy of the target's along-track position to be $\sigma_{x_{obj}} = 1$ m. The standard deviation of the road axis position $\sigma_{x_{road}}$ of the NavTeq data was estimated by comparing the vector data with precisely geocoded aerial images. The mean distance of the NavTeq axes from their corresponding reference was determined to be $\sigma_{x_{road}} = 3.5$ m (this result holds for high level roads like motorways). From this value, and by assessing the average length of the NavTeq polygon pieces, the accuracy of the road heading angle $\sigma_{\alpha_{road}}$ was deduced. For motorways its standard deviation results in $\sigma_{\alpha_{road}} = 2°$.

The accuracy of velocity estimates $\sigma_{\hat{v}_{mt}^{\Delta az}}$ is derived by inducting these empirical error measures into Equation (15). The resulting error $\sigma_{\hat{v}_{mt}^{\Delta az}}/v_{mt}$ is shown in Figure 9 as a function of heading angle α_{road} and normalized with the real target velocity v_{mt}. It can be seen from Figure 9 that the vehicles heading velocity v_{mt} can be estimated with a high accuracy of $\sigma_{\hat{v}_{mt}^{\Delta az}}/v_{mt} \leq 10\%$ if they were moving on roads with a heading angle of $\alpha_{road} \geq 4°$. For roads running nearly in along-track direction ($\alpha_{road} < 4°$) this approach fails to provide reliable velocity measures.
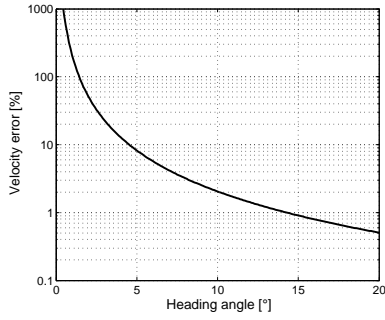
Figure 9: Relative velocity error $\sigma_{\hat{v}_{mt}^{\Delta az}}/v_{mt}$ estimated from along-track displacement as a function of heading angle α_{road}. Note the logarithmic scale.

4.3 Velocity Estimation from Along-track Blurring

Both of the already presented estimation methods fail to give a reliable velocity estimate for vehicles moving almost in along-track direction. To fill the gap we propose to use the along-track blurring effect for estimating along-track velocities. The functional dependence of the velocity estimate on unknown or uncertain parameters is given by:

$$\hat{v}_{mt}^x = -\sqrt{(v_{sat} - v_{mt}) \cdot cos(\hat{\alpha})^2 + y_0 \cdot \hat{a}_y \cdot sin(\hat{\alpha})} + v_{sat} \tag{16}$$

As explained in Section 2.1 both along-track velocity $v_x = v_{mt} \cdot cos(\alpha)$ and across-track acceleration a_y give rise to peak broadening in along-track. Usually, it is assumed that the acceleration of vehicles is zero during the time of illumination. As a consequence, actual occurring across-track accelerations introduce errors to the velocity estimates. According to empirical studies based on inertial navigation system measurements with cars driving on city streets and highways, accelerations up to $a_y = 2\ m/s^2$ are likely to happen in common traffic scenarios. Thus, we assume $\sigma_{a_y} = 2\ m/s^2$ as a "worst case" error source for the following calculations. Besides of possible acceleration, the standard deviation of the road heading angle $\sigma_{\alpha_{road}} = 2°$ influences the accuracy of the velocity estimate $\sigma_{\hat{v}_{mt}^x}$.

$$\sigma_{\hat{v}_{mt}^{\delta FM}} = \sqrt{\left(\frac{\partial \hat{v}_{mt}^{\delta FM}}{\partial \alpha_{road}}\right)^2 \sigma_{\alpha_{road}}^2 + \left(\frac{\partial \hat{v}_{mt}^{\delta FM}}{\partial a_y}\right)^2 \sigma_{a_y}^2} \tag{17}$$

Figure 10a) shows $\sigma_{\hat{v}_{mt}^{\delta FM}}$ as a function of real target velocity v_{mt} and real road heading α_{road}. The standard deviation of the velocity estimate is dominated by acceleration influences and increases with α_{road}. The dependence on v_{mt} is merely a secondary effect.
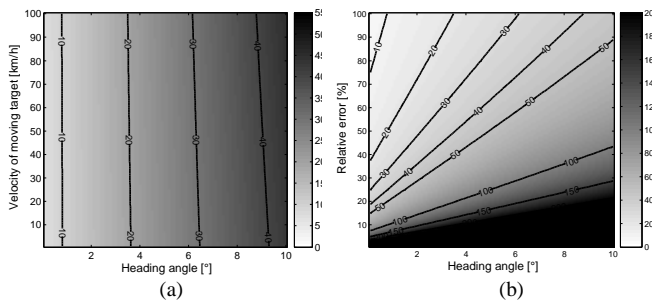
Figure 10: a) Standard deviation $\sigma_{\hat{v}_{mt}^x}$ of vehicle velocities estimated from along-track blurring as a function of target velocity v_{mt} and heading angle α_{road}. $\sigma_{\hat{v}_{mt}^x}$ is given in km/h. b) relative velocity error $\sigma_{\hat{v}_{mt}^x}/v_{mt}$.

For $\alpha_{road} < 4°$, i.e. for the heading angles of interest (see Sect. 4.2), the standard deviation $\sigma_{\hat{v}_{mt}^{\delta FM}}$ reaches up to 22 km/h. The relative error of the estimated velocities is indicated in Figure 10b). It indicates that the velocity of slow moving targets cannot be reliably estimated even for very small heading angles α_{road}, whereas the speed of fast moving targets can be estimated with better relative accuracy.

Sections 4.1 to 4.3 show that several possibilities exist to estimate the velocity of moving vehicles from TerraSAR-X data. According to the quality of the velocity estimates the usage of along-track displacement is the most promising approach for a wide range of heading angles α_{road}. If vehicles move nearly in along-track, the accuracy of velocity estimates is fair for all estimators. Still, the use of along-track blurring gives best results.

4.4 Examples

To demonstrate the quality of the velocity estimation for real live scenarios we calculated the expected standard deviation of the estimated velocity $\sigma_{\hat{v}_{mt}}$ for a road network north of Munich. In this area three large motorways are situated which are highly frequented during rush hours. We applied two different velocity estimators to this test, the displacement-based and the blur-based estimator. Real TerraSAR-X orbit and sensor parameters have been used in this simulation and an average speed of 100 km/h was assumed. The orientation of the motorways relative to the choosen TerraSAR-X orbit and the resulting $\sigma_{\hat{v}_{mt}}$ values for both estimators are show in Figures 11a) to 11c) (the corresponding flight direction of the satellite is indicated as well. The standard deviation of the displacement-based velocity estimate $\sigma_{\hat{v}_{mt}^{\Delta az}}$ is shown in Figure 11a) in km/h for all three motorways. It can be seen that vehicle velocities can be estimated with high accuracy for large parts of the road network. However, in areas where the road is oriented nearly in along-track, the estimation error increases dramatically. Figure 11b) shows that the second detector, which is based on the blurring of the impulse response, provides better results for this areas. Thus, in order to get an optimal estimation quality, we combine both methods depending on the relative orientation of road and satellite track. The performance of the combined estimator is shown in Figure 11c). With the presented algorithm velocities can be estimated with an accuracy better than 10 km/h for about 80 % of the investigated road network.

5 SUMMARY

A system to detect moving vehicles from TerraSAR-X data and to estimate their respective velocities has been presented. Besides a detailed description of the methods used, performance analyses are shown in addition. The detection of fast moving traffic seams to be very promising, whereas slow moving cars are hard to distinguish from non moving background. The estimation of the velocity of detected vehicles can be done with high accuracy for nearly all possible observation geometries. All approaches are subject to further improvement and a more detailed performance analysis will be presented as soon as the satellite is in its orbit.

ACKNOWLEDGEMENT

(a)

(b)

(c)

flight path
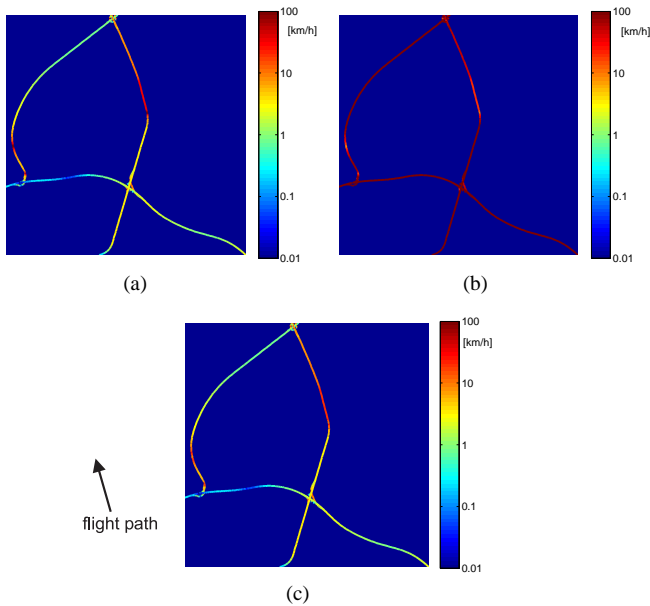
Figure 11: Simulation of $\sigma_{\hat{v}_{mt}}$ for a road network north of Munich ($v_{mt} = 100$ km/h assumed). a) shows the estimation accuracy for a displacement-based detector, b) for a blur-based detector, and c) indicates the estimation quality if both detectors are combined.

REFERENCES

Bamler, R. and Schättler, B., 1993. SAR Data Acquisition and Image Formation. In: G. Schreier (ed.), Geocoding: ERS-1 SAR Data and Systems, Wichmann-Verlag.

Breit, H., Eineder, M., Holzner, J., Runge, H. and Bamler, R., 2003. Traffic Monitoring using SRTM Along-Track Interferometry. In: Proc. of IGARSS03, Vol. 2, pp. 1187–1189.

Cumming, I. and Wong, F., 2005. Digital Processing of Synthetic Aperture Radar Data. Artech House, Boston.

Gierull, C., 2001. Statistics of SAR interferograms with application to moving target detection. Technical Report DREO-TR-2001-045, Defence R&D Canada.

Gierull, C., 2002. Moving target detection with along-track sar interferometry. a theoretical analysis. Technical Report DRDC-OTTAWA-TR-2002-084, Defence R&D Canada.

Gierull, C., 2004. Statistical analysis of multilook SAR interferograms for CFAR detection of ground moving targets. IEEE Transactions on Geoscience and Remote Sensing 42, pp. 691–701.

Hinz, S., 2005. Fast and Subpixel Precise Blob Detection and Attribution. In: Proceedings of ICIP'05, Genua, on CD.

Joughin, I., Winebrenner, D. and Percival, D., 1994. Probability density functions for multilook polarimetric signatures. IEEE Transactions on Geoscience and Remote Sensing 32(2), pp. 562–574.

Klemm, R., 1998. Space-time adaptive processing. The Institute of Electrical Engineers, London, UK.

Lee, J.-S., Hoppel, K. and Mango, S., 1994. Intensity and Phase Statistics of Multilook Polarimetric and Interferometric SAR Imagery. IEEE Transactions on Geoscience and Remote Sensing 32(5), pp. 1017–1028.

Leitloff, J., Hinz, S. and Stilla, U., 2005. Automatic Vehicle Detection in Space Images Supported by Digital Map Data. In: ISPRS/DAGM joint Workshop on City Models, Road Databases, and Traffic Monitoring, CMRT05, Vienna.

Livingstone, C.-E., Sikaneta, I., Gierull, C.-H., Chiu, S., Beaudoin, A., Campbell, J., Beaudoin, J., Gong, S. and Knight, T.-A., 2002. An Airborne Sythentic Apertur Radar (SAR) Experiment to Support RADARSAT-2 Ground Moving Target Indication (GMTI). Canadian Journal of Remote Sensing 28(6), pp. 794–813.

Meyer, F. and Hinz, S., 2004. The Feasibility of Traffic Monitoring with TerraSAR-X - Analyses and Consequences . In: International Geoscience and Remote Sensing Symposium, pp. 1502–1505.

Meyer, F., Hinz, S., Laika, A. and Bamler, R., 2005. A-Priori Information Driven Detection of Moving Objects for Traffic Monitoring by Spaceborne SAR. In: Proc. of CMRT05, International Archives of Photogrammetry, Remote Sensing and Spatial Information Sciences, Vol. XXXVI, 3/W24, pp. 89–94.

Sharma, J., Gierull, C. and Collins, M., 2006. Compensating the effects of target acceleration in dual-channel SAR-GMTI. IEE Radar, Sonar, and Navigation.

Sikaneta, I. and Gierull, C., 2005. Two-Channel SAR Ground Moving Target Indication for Traffic Monitoring in Urban Terrain. In: Proc. of CMRT05, International Archives of Photogrammetry, Remote Sensing and Spatial Information Sciences, Vol. XXXVI, 3/W24, pp. 95–101.

Suchandt, S., Eineder, M., Mueller, R., Laika, A., Hinz, S., Meyer, F., Breit, H. and Palubinskas, G., 2006. A GMTI processing system for the extraction of traffic information from TerraSAR-X data. European Conference on Synthetic Aperture Radar EUSAR'06 p. in print.

Ulaby, F. and Dobson, M., 1989. Handbook on Radar Scattering Statistics for Terrain. Artech House, Boston.

Weihing, D., Hinz, S., Meyer, F., Laika, A. and Bamler, R., 2006. Detection of along-track ground moving targets in high resolution spaceborne SAR images. International Archives of Photogrammetry and Remote Sensing, Congress Enschede, Commission VII.